ACS APPLIED ENERGY MATERIALS

www.acsaem.org Article

Degradation Analysis of Triple-Cation Perovskite Solar Cells by Electrochemical Impedance Spectroscopy

Jeevan Torres, Isaac Zarazua, Diego Esparza,* Jesús Manuel Rivas, Michael Saliba, Iván Mora-Seró, Silver-Hamill Turren-Cruz,* and Antonio Abate

Cite This: *ACS Appl. Energy Mater.* 2022, 5, 12545−12552 Read Online

ACCESS | Metrics & More | Article Recommendations | Supporting Information

ABSTRACT: In this work, the electrical properties of different triple-cation compositions with the formula $Cs_{0.05}FA_{1-X}MA_XPb(I_{1-X}Br_X)_3$ have been analyzed using electrochemical impedance spectroscopy. The perovskite solar cells were subjected to ambient conditions to compare their results in terms of ambient degradation. Their morphology, optical properties, and photovoltaic performance were characterized. We analyzed the causes and effects of ambient degradation mechanisms on the devices. Electrochemical processes such as ion movement, a combination of radiative recombination and nonradiative recombination, and charge transport were detected. The MA percentage decrease in the composition of triple-cation perovskites, $APbX_3$ produces an improvement in the stability and durability of perovskite solar cells. This enhancement is due to the reduction of the amount of ion vacancies helping to reduce the degradation in the device by avoiding the accumulation of defects.

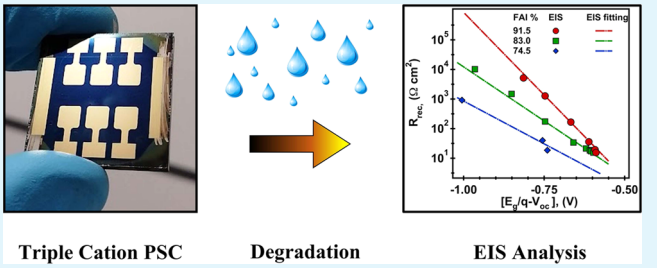

KEYWORDS: *perovskite solar cells, impedance spectroscopy, charge transport, recombination, stability, degradation, ion movement*

INTRODUCTION

Perovskite solar cells (PSCs) have been the main focus of attention for photovoltaic materials in the last decade. This is due to their excellent optoelectronic properties and high efficiencies. These properties include high absorption over the visible spectrum,[1] low exciton binding energy,[2] balanced charge transport properties with long diffusion lengths,[3,4] and a tunable band gap from 1.1 to 2.3 eV by interchanging cations,[5] metals,[6] and/or halides.[7] In just 12 years, PSCs have improved from 3.8%[8] (2009) of power conversion efficiency (PCE) to over 25%[9] (2021).

Halide perovskites (PVSKs) in solar cells have a general structure of ABX_3, where A represents an organic or inorganic monovalent cation such as cesium (Cs^+), methylammonium (MA^+), or formamidinium (FA^+); B is a divalent metal such as Pb^{2+} or Sn^{2+}; and X is a halide such as I^-, Br^-, or Cl^-.[10,1110,11] $CH_3NH_3PbI_3$ (MAPI) is the most studied PVSK compound for being one of the first to be used in sensitized solar cells,[8] later introduced in single-junction solar cells by Snaith et al.[12] Being a hybrid material (organic−inorganic), the principal problem in these solar cells has been the stability by degradation.[13,14] MAPI is a hybrid material that has a structural phase transition at 55 °C.[6] MAPI stability is limited and affected by different parameters such as humidity, temperature, and UV light.[15−18]

For this reason, new PVSK compounds are studied to increase the photoconversion efficiency, reproducibility, and stability.[15,16] The stability is related to the degradation of the active film, and this is affected by thermal and humid stability conditions.[17−19] In recent years, research has been led to find the best combination of elements to obtain highly efficient and stable PVSKs.[15] For the A cation, MA, FA, Cs, Rb, or K is used,[20−24] while in the B metal position, Pb or Sn is commonly used.[25] In the case of the halide component, iodide, bromide, or chloride is used.[26,27] Saliba et al. incorporated Cs into the $FAMAPbI_{1-X}Br_X$ PVSK, and this multication approach has been extensively used for its good efficiency and stability,[28,29] thus creating the so-called triple-cation PVSK ($CsFAMAPbI_{1-X}Br_X$).[21] This resulted in a significant improvement in the stability of the PVSK without compromising too much of its efficiency. As a result, this type of PVSK has become a standard for the manufacturing of PSCs.[30,31] Triple-cation PVSKs, however, are still not stable enough to withstand adverse environmental conditions; therefore, stability continues to be the main problem of PSCs.

Electrochemical impedance spectroscopy (EIS) is a well-known technique for characterizing electrochemical processes in different types of solar cell technologies.[14,32−34] EIS captures the current response to small amplitude modulating the voltage

Received: July 11, 2022
Accepted: August 29, 2022
Published: October 7, 2022

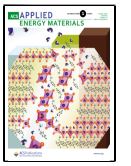

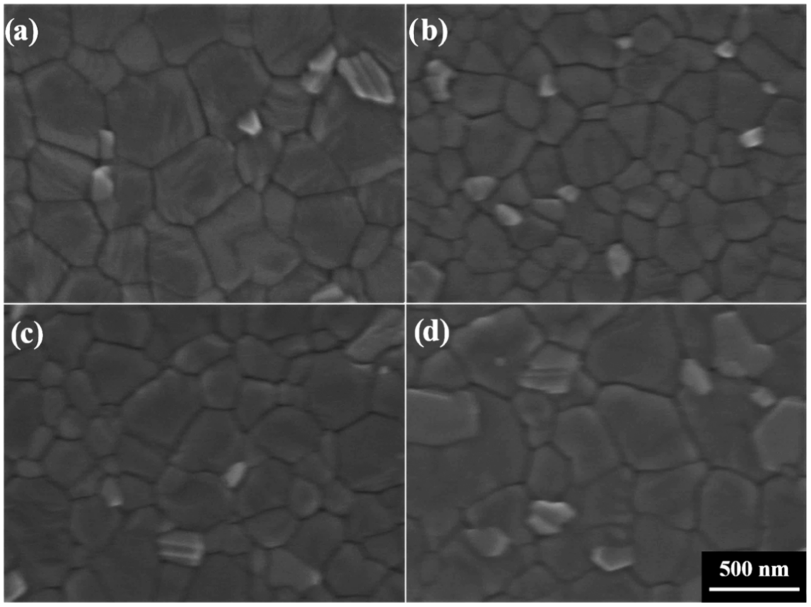

Figure 1. SEM images of the $Cs_{0.05}FA_{1-X}MA_XPb(I_{1-X}Br_X)_3$ perovskite thin films varying the FAPI concentration at (a) 100%, (b) 91.5%, (c) 83%, and (d) 74.5%.

stimulus. To interpret the data generated by this method, an equivalent circuit comprising resistive and capacitive response elements is used for fitting. For a correct interpretation, different elements of the circuit have to be correlated with the physical mechanisms of the device.[32,35] With the correct interpretation, representing physical processes into circuit elements, we can have a better understanding of the causes and effects of both degradation mechanisms and physical processes occurring in the PSC.[32]

In this work, the effects of ambient degradation exposure on triple-cation PSCs are analyzed. PSCs with the configuration $Cs_{0.05}FA_{1-X}MA_XPb(I_{1-X}Br_X)_3$ were fabricated varying the $FAPbI_3$ (FAPI) molar concentration at values of 100, 91.5, 83, and 74.5%. For simple labeling, we will refer to each combination by the amount of FAPI in the triple-cation perovskite, having 100, 91.5, 83, and 74.5% of FAPI in the PVSK film. The maximum PCE obtained before degradation was 18.55%, observed in the samples with 83% of FAPI. After the PSCs were stored at a relative humidity of about 50%, in the dark and at ambient temperature fluctuating between 20 and 40 °C during 90 days, the PSCs with 91.5% of FAPI content showed the best performance (PCE of 14%). The EIS results indicate a reduction in the recombination processes with an increase in the FAPI concentration. The ideality factor "m" and R_0 suggest that the reduction in the FAPI content promotes the creation of recombination paths. Meanwhile, the R_{dr} resistance indicates that an increase in recombination paths is due to an increase in the formation of ion vacancies as the FAPI concentration is reduced.

EXPERIMENTAL SECTION

Materials. Patterned fluorine tin oxide (FTO)-coated glass substrates, lead iodide (PbI_2, TCI, 99.99%), lead bromide ($PbBr_2$, TCI, 99.99%), formamidinium iodide (FAI, Dyenamo, >99%), methylammonium iodide (MAI, Dyenamo, >98%), and cesium iodide (CsI, Aldrich, 99.9%) were used as purchased. In addition, spiro-MeOTAD (Lumtec, LT-S922, 99%), *N*,*N*-dimethylformamide (DMF, Aldrich, anhydrous 99.8%), dimethyl sulfoxide (DMSO, Aldrich, 99.9%), isopropanol (IPA, Aldrich, anhydrous 99.5%), lithium salt (LiTFSI, Aldrich, 99.95%), acetone, acetonitrile, ethanol, and acetylacetone ($CH_3COCH_2COCH_3$, Honeywell, ≥99.5%) were also used as purchased.

Device Fabrication. FTO-coated glass substrates were sequentially cleaned in detergent, deionized water, acetone, and IPA. The first deposition was a compact TiO_2 film, deposited by spray pyrolysis. Then, a mesoporous TiO_2 film was deposited by spin coating at 2000 rpm for 10 s and annealed at 450 °C for 2 h. Passivation with lithium salt was done with LiTFSI dissolved in acetonitrile 10 mg mL^{-1}, spin coated at 1000 rpm for 10 s, and heat-treated similarly to mesoporous TiO_2. A DMF/DMSO (4:1, V:V) solvent was used to dissolve PbI_2 and $PbBr_2$ in 1.5 M concentration, to be added onto FAI and MABr at 1.24 M concentration, respectively. CsI was used as a dopant dissolved in DMSO at 1.5 M concentration. Mixed perovskites were prepared according to the experiments. Then, spiro-MeOTAD was spin coated at 1800 rpm for 30 s. Finally, an 80 nm gold film was thermally evaporated as a metal electrode.

Characterization. *Current Density–Voltage (J–V) Curves.* The *J–V* curves of the PSCs were recorded using a Wavelabs Sinus-70 LED class AAA solar simulator in air. The light intensity was calibrated with a silicon reference cell from Fraunhofer ISE. *J–V* scans were performed with a Keithley 2400 SMU, controlled by a measurement control program written in LabView. A voltage step of 10 mV with an integration time of 50 ms per point and settling time of 50 ms after voltage application was used. This corresponds to a scan rate of 100 mV s^{-1}. The active area of the device is 0.16 cm^2.

Scanning Electron Microscopy (SEM). SEM images were recorded with a Hitachi S-4100 at an accelerating voltage of 5 kV.

Electrochemical Impedance Spectroscopy (EIS). EIS measurements were performed under different light irradiances fixing a DC voltage equal to V_{oc} at the chosen irradiance and applying AC perturbations of 10 mV with a frequency scan from 10^5 to 10^{-1} Hz.

UV–Vis Spectroscopy. Light transmittance of the samples was performed with a Perkin Elmer LAMBDA 1050 UV/VIS spectrometer. Samples for the UV–Vis measurements were prepared using a stack consisting of FTO/compact TiO_2/mesoporous TiO_2/perovskite.

RESULTS AND DISCUSSION

Morphology Characterization. Figure 1 shows SEM images of the $Cs_{0.05}FA_{1-X}MA_XPb(I_{1-X}Br_X)_3$ perovskite thin films varying the FAPI concentration at 100, 91.5, 83, and

https://doi.org/10.1021/acsaem.2c02161
ACS Appl. Energy Mater. 2022, 5, 12545−12552

74.5%. The sample with 100% of FAPI shows a homogeneous film (Figure 1a) without pinholes, with regular interfaces between grains, and an average grain size of about 315 ± 5.2 nm (see Figure S1). The reduction of FAPI (91.5%) and the introduction of 8.5% $MAPbBr_3$ (MAPBr) produce a somewhat less homogeneous film (Figure 1b) with a reduced average grain size (223 ± 11.3 nm), the smallest gain size of all four PVSKs studied. In the case of the sample with 83% of FAPI, they produce a homogeneous film (Figure 1c) with a decreased grain boundary interface area due to the larger grain size. The average grain size of this sample is about 236 ± 6.7 nm. Finally, the perovskite film with 74.5% of FAPI (Figure 1d) shows a homogeneous film, also without pinholes, and an average grain size of 312 ± 6.6 nm.

Optical Properties. Figure 2 shows the absorption spectra of the $Cs_{0.05}FA_{1-X}MA_XPb(I_{1-X}Br_X)_3$ perovskite thin films of

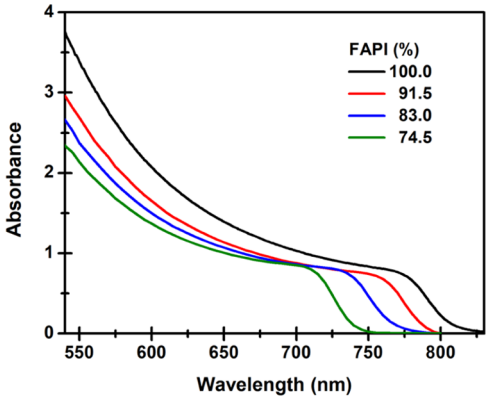

Figure 2. Absorption spectra of the $Cs_{0.05}FA_{1-X}MA_XPb(I_{1-X}Br_X)_3$ perovskite thin films varying the FAPI concentration at 100, 91.5, 83, and 74.5%.

the samples under study. In the sample with 100% FAPI, the absorption begins to rise near 850 nm, indicating a band gap of about 1.53 eV (Figure S2). When the amount of FAPI is reduced to 91.5%, a general reduction of the absorbance is obtained; this could be indicating that there will be a reduction in the photogeneration process.[36] At the same time, the absorption range is reduced from 800 to 780 nm, indicating an increase of the band gap to 1.58 eV, which is an expected consequence of the partial substitution of FAPI by MAPBr.[37] This trend, with reductions of both absorbance intensity and absorption range, is followed by the samples with a lower amount of FAPI, resulting in band gaps of 1.63 and 1.68 eV for the samples with 83 and 74.5%, respectively.

Photovoltaic Characterization. Figure 3 shows the $J-V$ curves of the best fresh samples for each FAPI concentration. Figure 4 shows the statistical values of the photovoltaic parameters of 15 samples for each FAPI concentration. The corresponding statistical value for each parameter is shown in Table S1. The PSCs with an FAPI concentration of 100% have an average short-circuit current density (J_{sc}) of 21.2 ± 0.6 mA cm^{-2}, an open-circuit voltage (V_{oc}) of 0.941 ± 0.012 V, and a fill factor (FF) of 72.8 ± 4.1%, resulting in a PCE of 14.7 ± 0.7%. When the FAPI concentration is reduced to 91.5%, J_{sc} is reduced to 21.0 ± 0.2 mA cm^{-2} and the FF increases to 76.3 ± 2.4%. Meanwhile, the V_{oc} increases almost linearly with the reduction of FAPI, resulting in an enhanced PCE of 16.2 ± 0.6%. The J_{sc} trend is consistent with the observed reduction in the light absorption in the absorption spectra (Figure 2). The

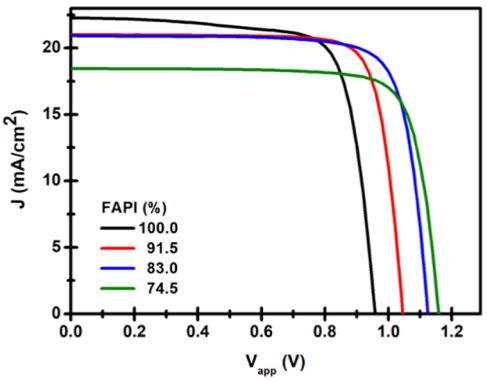

Figure 3. $J-V$ curves of fresh samples of $Cs_{0.05}FA_{1-X}MA_XPb(I_{1-X}Br_X)_3$ perovskite thin films varying the FAPI concentration at 100, 91.5, 83, and 74.5%.

V_{oc} increases with the reduction of the FAPI concentration to 83%. V_{oc} is 1.108 ± 0.024 V and the best PCE is 17.6 ± 0.7%. Finally, in the samples with an FAPI concentration of 74.5%, J_{sc} is reduced to 18.1 ± 0.5 mA cm^{-2}, V_{oc} is 1.134 ± 0.028 V, and the FF is 73.8 ± 5.5%, obtaining an average PCE of 15.1 ± 1.2%. As expected from the progressive increase in band gap (E_g), J_{sc} decreases as the content of MA increases, see Figure 4. V_{oc} follows an inverse trend with a clear increase as the FAPI concentration decreases. Note that the increase in V_{oc} is higher than the increase in the perovskite E_g, see Table S2. For example, for the sample with the FAPI concentration of 74.5%, the increment of E_g with respect to the FAPI concentration of 100% is 0.15 eV, while the increment in average V_{oc} is 0.193 V, see Table S2. This difference can be attributed to a decrease of the nonradiative recombination as the MA content in fresh samples increases.

PSCs after 90 Days from Device Fabrication. The PSCs were stored away in the dark, at ambient temperature fluctuating between 20 and 40 °C, and at a relative humidity of about 50%, for 90 days after device fabrication. The samples were kept at these ambient conditions without encapsulation or sealing. The PCE of the devices was affected after degradation according to the ratio of FAPI to MAPBr in the perovskite film.

Figure 5 shows the $J-V$ curves of the samples after 90 days of device fabrication and stored under ambient conditions. The samples with 100% of FAPI did not show photovoltaic behavior after 90 days from device fabrication. The solar cell parameters of the degraded devices are collected in Table S3. Here, it can be seen that the rest of the samples have, on average, short-circuit currents greater than 15.5 mA cm^{-2} and voltages greater than 1 V. It can be observed in the curves that the sample with 91.5% of FAPI content is the one with the best performance, mainly for having higher J_{sc} in comparison to other samples. However, the samples with 91.5% of FAPI have an average PCE value 27% lower than the initial average PCE value. Reducing the FAPI content to 83% produces a significant reduction in average PCE of 43% with respect to the PCE value for fresh samples. In addition, the average FF decreases considerably for this FAPI concentration, see Table S3. This fact can be due to three causes: (1) Increase in load leakage processes. (2) Resistance to transport of charge carriers. At first glance, there seems to be a change in the series resistance; however, additional analysis is required to evaluate this fact. (3) Ideality factor, related to the type of

https://doi.org/10.1021/acsaem.2c02161
ACS Appl. Energy Mater. 2022, 5, 12545−12552

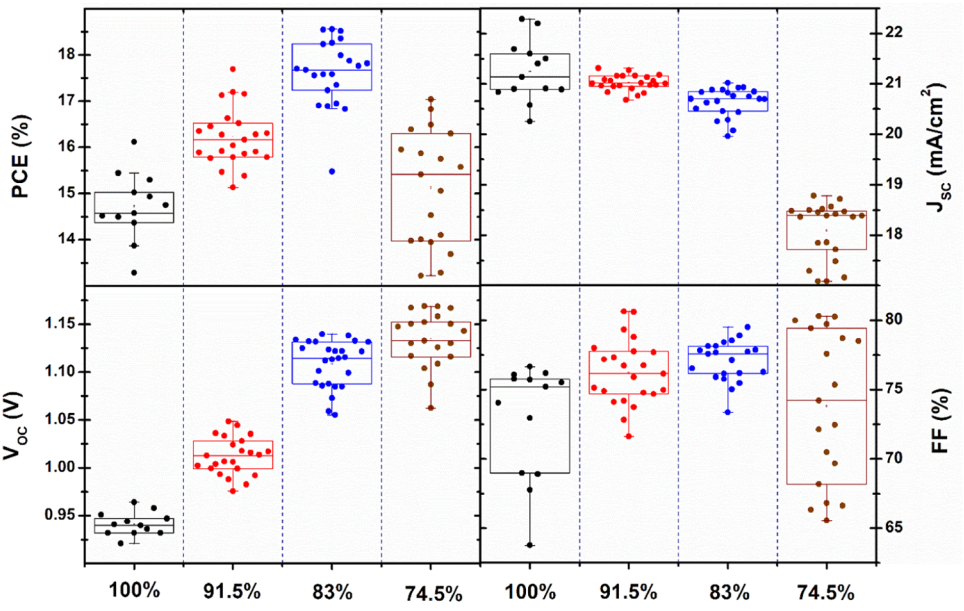

Figure 4. Statistical values of the photovoltaic parameters of 15 samples for $Cs_{0.05}FA_{1-X}MA_XPb(I_{1-X}Br_X)_3$ perovskite thin films varying the FAPI concentration at 100, 91.5, 83, and 74.5%.

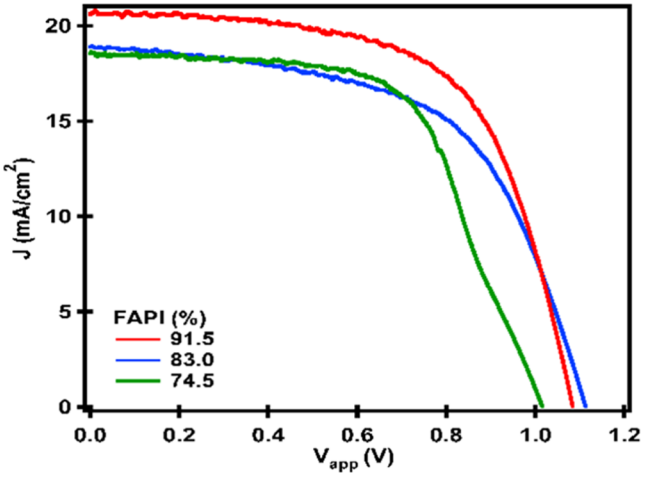

Figure 5. $J-V$ curves after 90 days from device fabrication of $Cs_{0.05}FA_{1-X}MA_XPb(I_{1-X}Br_X)_3$ perovskite thin films varying the FAPI concentration at 91.5, 83, and 74.5%.

recombination, is one of the issues that are expected to change during degradation. Each one of these parameters can be evaluated with an electrochemical impedance spectroscopy study.

Electrochemical Impedance Spectroscopy (EIS). To clarify how the working mechanisms of the cells were affected by the degradation processes, EIS measurements at open-circuit conditions and different irradiances were performed.[38] Figure 6a shows the Nyquist plot for the sample with 91.5% of FAPI. For samples with 83 and 74.5% of FAPI, Nyquist plots are illustrated in Figure S3. Here, it is observed that all impedance spectra have two well-defined arcs that exponentially decrease with the irradiance. All of the studied samples show similar impedance trends. The semicircles are usually stated as high- (left ones) and low-frequency (right ones) arcs. The total contribution of both arcs (the addition of the diameters) has been related to the recombination resistance, R_{rec}, of the PSC,[32,33,39] considering that the transport resistance is negligible. The impedance of PSC is strongly affected by ion motion mostly in the low frequency range.[40]

To analyze the impedance pattern, we used the equivalent circuit formalism fitting the experimental results with the equivalent circuit plotted in Figure 6b. This circuit is one of the most extended models and provides results that can be correlated with other models including the circuit with elements arranged in series[35,40] or as an alternative model to a circuit using transistors.[42] In this circuit, R_s stands for the series resistance, and it is related to the FTO and the resistance of the wire connections. C_g is the geometric capacitance (associated with the dielectric properties of the perovskite). R_{rec} is the resistance determined by the sum of the arc diameters. R_{dr} and C_{dr} are dielectric relaxation (dr)-like resistance and capacitance of the perovskite, respectively. These circuit elements have not been completely related to a single physical process but influenced by several ones. R_{dr} is associated with the recombination mechanism and influenced by electron diffusion and ion vacancies.[40] Meanwhile, C_{dr} has been previously studied and associated with the charge accumulation at the interfaces, being the principal cause of $J-V$ PSC hysteresis,[43] although different ion parameters affect its value.[40] Figure 6c shows R_{rec} values obtained from impedance fitting for the degraded samples under different illuminations at V_{oc} conditions as a function of $E_g/q - V_{oc}$, where q is the electron charge. This representation allows us to compare R_{rec} removing the effect of the different band gaps.[41] It can be observed that, on one hand, the sample with 74.5% has a lower R_{rec} value than the other samples. The R_{rec} values of samples with different concentrations get closer in the high V_{oc} region. This fact explains the lower V_{oc} observed for the 74.5% sample as a consequence of the higher recombination rate in this sample. On the other hand, all of these samples show different slopes in Figure 6c. The slope of R_{rec} is determined by the ideality factor "m," which is closely related to this kind of recombination process,[44−47] following the general expression in eq 1

https://doi.org/10.1021/acsaem.2c02161
ACS Appl. Energy Mater. 2022, 5, 12545−12552

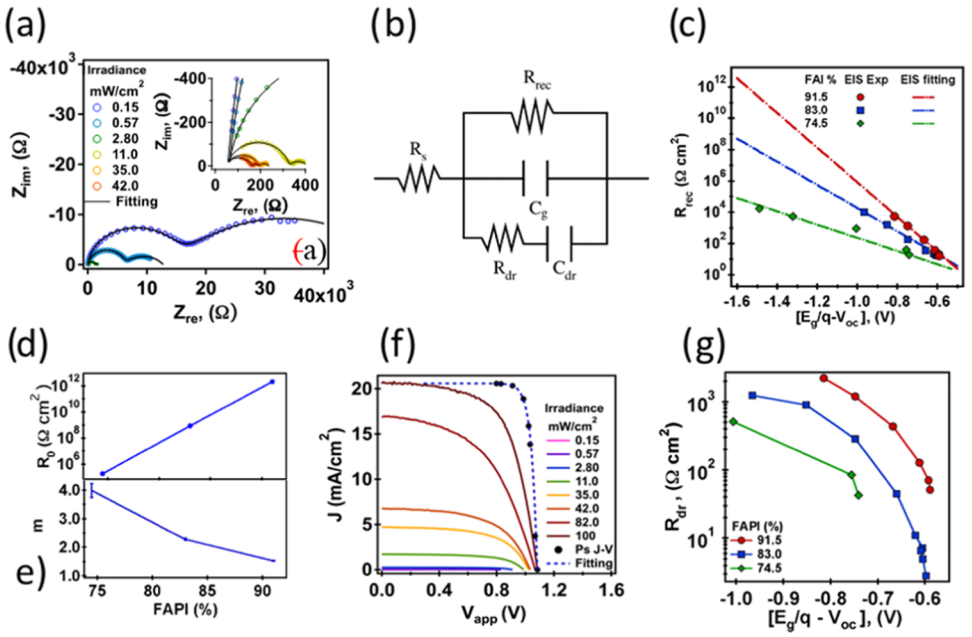

Figure 6. (a) Nyquist plot of the impedances for the sample with 91.5% of FAPI measured under open-circuit conditions at several irradiances. (b) Circuit used to fit the impedance spectra.[39] (c) Recombination resistance vs open-circuit voltage corrected by the optical band gap.[41] (d) Recombination resistance at $V = 0$. (e) Ideality factor "m." (f) $J-V$ curves of the 91.5% of FAPI sample at several irradiances showing the pseudo $J-V$ curve (Ps $J-V$). (g) Dielectric relaxation resistance.

Table 1. Calculated Values of R_{rec}, m, R_s, and R_{sh}

	EIS		pseudo $J-V$			$J-V$		V_{oc}
FAPI (%)	$R_0(\Omega\ cm^2)$	m	$R_0(\Omega\ cm^2)$	m	$R_s(\Omega\ cm^2)$	$R_0(\Omega\ cm^2)$	m	m
91.5	2.15×10^{12}	1.52	1.55×10^{12}	1.52	7	1.17×10^{4}	5.68	1.54
83.0	8.49×10^{8}	2.27	3.87×10^{8}	2.33	10	3.07×10^{3}	7.53	2.58
74.5	1.72×10^{5}	3.98	2.16×10^{5}	3.77	13	2.92×10^{3}	7.52	5.54

$$R_{rec} = R_0 e^{-qV/mk_BT} \tag{1}$$

where R_0 is the recombination resistance at $V = 0$, k_B is the Boltzmann constant, and T is the temperature. Note that in the case of PSCs, this ideality factor is also affected by the ionic movement. For the sake of clarity, we differentiate this ideality factor from other solar cells, where it is just determined by electron dynamics. Hereafter, we will call "m" the apparent ideality factor of PSCs.[40,48,49] The ideality factor can be related to the recombination mechanism.[50] Also, it has been recently used to track the performance of PSCs outdoors.[47]

Beyond the interpretation of the apparent ideality factor, which we will discuss later, this parameter can be obtained independently through different measurements. Consequently, it is a good parameter to evaluate the consistency of electrical characterization. For instance, "m" can be calculated from eq 1 considering the R_{rec} obtained by EIS, as well as R_0, see Table 1 and Figure 6d,e. In addition, the apparent ideality factor can be easily obtained from the dependence of V_{oc} with light intensity, following the general expression in eq 2

$$V_{oc} = \frac{mk_BT}{q} \ln\left(\frac{J_{ph}}{J_0}\right) \tag{2}$$

where J_{ph} is the photogenerated current at the chosen light intensity and J_0 the reverse saturation current.

Eventually, "m" can also be obtained from the $J-V$ curve using the diode equation, following the general expression in eq 3

$$J = J_{sc} - \frac{mk_BT}{qR_0}(e^{qV/mk_BT} - 1) \tag{3}$$

From Table 1, it can be appreciated that there is a good agreement between "m" values calculated with eqs 1 and 2, while there is a clear discrepancy with "m" values calculated from the $J-V$ curve using eq 3. This discrepancy is due to the effect of shunt and series resistance in the $J-V$ curve that affects the $J-V$ pattern. If $J-V$ is recalculated, removing the effect of these resistances, a pseudo $J-V$ curve can be obtained, see Figure 6f. The pseudo $J-V$ curves were constructed by applying eq 4[51,52]

$$J_{V_{oc}\Phi} = J_{sc\Phi_{1\ sun}}\left(1 - \frac{\Phi}{\Phi_{1\ sun}}\right) \tag{4}$$

where Φ is the irradiance and $\Phi_{1\ sun}$ corresponds to the irradiance at AM1. Standard (100 mW cm^{-2}) $J_{sc\Phi_{1\ sun}}$ is the short-circuit current density measured at 1 sun. $J_{V_{oc}\Phi}$ and $V_{oc\Phi}$ are the current density and voltage couple calculated for each irradiance, respectively. The resulting points (black circles in Figure 6f) correspond to the response of the cell without the series resistance, as in open-circuit conditions, no current is

https://doi.org/10.1021/acsaem.2c02161
ACS Appl. Energy Mater. 2022, 5, 12545−12552

flowing in the devices and only recombination and photogeneration processes are reflected.[51,52]

Note that "m" calculated from the pseudo $J-V$ curve shows a good agreement to the apparent ideality factor obtained from eqs 1 and 2, as it should be expected (see Table 1 and Figure 6e). This independent determination of "m" strengthens the consistency of the electrical characterization. On one hand, this calculation provides validity to the R_{rec} obtained and, consequently, of the equivalent circuit used, see Figure 6b. On the other hand, it stresses the fact that no significant degradation occurred during electrical characterization.

Figure 6d,e shows R_0 and "m," respectively, calculated from eq 1, fitting the experimental results plotted in Figure 6c. The evolution of these parameters with the FAPI content can be clearly observed for the degraded samples. The sample with 91.5% of FAPI, the one that showed the smallest amount of degradation, in comparison with fresh samples, has an "m" value of 1.52. Values of an apparent ideality factor between 1 and 2 are commonly observed in PSCs. In the most general case, this range indicates that the recombination is affected by both Shockley–Reed–Hall recombination, through a single state bulk recombination, and surface recombination.[45,50] When the amount of FAPI is reduced to 83%, "m" increases to 2.27, implying a predominant Shockley–Reed–Hall bulk recombination process characterized by an apparent ideality factor of 2. Finally, when the FAPI content is reduced to 74.5%, "m" increases to more than 3.9, indicating a much complex recombination process through multiple energy levels, indicating a massive formation of defects.[44−47,50] Meanwhile, the evolution of R_0 (see Figure 6d) exponentially decreases with the amount of FAPI, indicating the apparition of parallel current paths originated by defects, increasing the nonradiative recombination processes and reducing the performance of the solar cells.

To characterize the effect of degradation in the ionic behavior, the R_{dr} resistances of different samples are compared in Figure 6g. Note that R_{dr} decreases with the amount of FAPI. This is an indicator of higher density of ion vacancies and/or a higher ion diffusion coefficient.[40] In our case, it can be associated with the higher density of ion vacancies as there is also an increase in C_{dr}, see Figure S5, while in the case of the higher ion diffusion coefficient, a decrease of C_{dr} should be expected.[40] This result points out to the fact that the decrease of the FAPI concentration makes the system more prone to increase ion vacancies and, consequently, to increase the density of defects and the degradation of the sample.

CONCLUSIONS

We analyzed the effect of ambient degradation exposure of triple-cation PSCs with different ratios of mixed cations and halides. The maximum PCE obtained before the degradation was at 18.55% with the configuration of FAPI at 83%. When the PSCs were stored for 90 days at ambient conditions, it was observed that the sample with the configuration $Cs_{0.05}FA_{91.5}MA_{8.5}Pb(I_{1-0.85}Br_{0.85})_3$ showed the best PCE performance (~16%). EIS was used to elucidate the causes and effects of the degradation mechanisms in the solar cells. Perovskites without MABr degrade much faster than those containing this material. Therefore, we conclude that the MABr content in perovskites has an stabilizing effect under extreme degradation conditions. In addition, the EIS results show higher recombination rates for samples with a lower content of FAPI. The apparent ideality factor "m" and R_0 indicate that the reduction in the FAPI content promotes the formation of perovskite defects, increasing, in this way, the nonradiative recombination processes and reducing the performance of the solar cell. The R_{dr} resistance indicates that the defect density increases as the percentage of FAPI in the samples decreases due to a more prominent increase in ion vacancies during the degradation process. Determination of "m," with different independent measurements, allows us to ensure the consistency of the model and of the experimental characterization. Finally, EIS has provided important information about the source of degradation while highlighting its potential use for the understanding of the physical processes occurring in perovskite solar cells.

ASSOCIATED CONTENT

Supporting Information

The Supporting Information is available free of charge at https://pubs.acs.org/doi/10.1021/acsaem.2c02161.

Particle size histogram, Tauc plot, band gap V_{oc} relation, statistics of photovoltaic performance, resistance and capacitance trends, $J-V$ curves, and Nyquist plot graphs (PDF)

AUTHOR INFORMATION

Corresponding Authors

Diego Esparza − *Unidad Académica de Ingeniería Eléctrica, Universidad Autónoma de Zacatecas, Zacatecas, ZAC 98060, Mexico*; Email: desparza@uaz.edu.mx

Silver-Hamill Turren-Cruz − *Institute of Advanced Materials (INAM), University Jaume I, 12071 Castellón de la Plana, Spain; Young Investigator Group Active Materials and Interfaces for Stable Perovskite Solar Cells, Helmholtz-Zentrum Berlin für Materialien und Energie, 12489 Berlin, Germany*; orcid.org/0000-0003-3191-6188; Email: turren@uji.es

Authors

Jeevan Torres − *Unidad Académica de Ingeniería Eléctrica, Universidad Autónoma de Zacatecas, Zacatecas, ZAC 98060, Mexico; Institute of Advanced Materials (INAM), University Jaume I, 12071 Castellón de la Plana, Spain; Young Investigator Group Active Materials and Interfaces for Stable Perovskite Solar Cells, Helmholtz-Zentrum Berlin für Materialien und Energie, 12489 Berlin, Germany*

Isaac Zarazua − *Centro Universitario de los Lagos, Universidad de Guadalajara, Lagos de Moreno, JAL 47460, Mexico*; orcid.org/0000-0002-5722-7068

Jesús Manuel Rivas − *Unidad Académica de Ingeniería Eléctrica, Universidad Autónoma de Zacatecas, Zacatecas, ZAC 98060, Mexico*; orcid.org/0000-0002-5021-4942

Michael Saliba − *Institute for Photovoltaics, University of Stuttgart, 70569 Stuttgart, Germany*; orcid.org/0000-0002-6818-9781

Iván Mora-Seró − *Institute of Advanced Materials (INAM), University Jaume I, 12071 Castellón de la Plana, Spain*; orcid.org/0000-0003-2508-0994

Antonio Abate − *Young Investigator Group Active Materials and Interfaces for Stable Perovskite Solar Cells, Helmholtz-Zentrum Berlin für Materialien und Energie, 12489 Berlin, Germany*; orcid.org/0000-0002-3012-3541

Complete contact information is available at: https://pubs.acs.org/10.1021/acsaem.2c02161

Notes

The authors declare no competing financial interest.

■ ACKNOWLEDGMENTS

S.-H.T.-C. would like to thank the Spanish Ministry of Economy, Industry and Competitiveness (postdoctoral contract Juan de la Cierva Formación FJC2019-041835-I) for the financial support during this work. This work was performed under the auspices of the Universidad Autónoma de Zacatecas.

■ REFERENCES

(1) Jung, H. S.; Park, N.-G. Perovskite Solar Cells: From Materials to Devices. *Small* **2015**, *11*, 10−25.
(2) Lin, Q.; Armin, A.; Nagiri, R. C. R.; Burn, P. L.; Meredith, P. Electro-Optics of Perovskite Solar Cells. *Nat. Photonics* **2015**, *9*, 106−112.
(3) Stranks, S. D.; Eperon, G. E.; Grancini, G.; Menelaou, C.; Alcocer, M. J. P.; Leijtens, T.; Herz, L. M.; Petrozza, A.; Snaith, H. J. Electron-Hole Diffusion Lengths Exceeding 1 Micrometer in an Organometal Trihalide Perovskite Absorber. *Science* **2013**, *342*, 341−344.
(4) Dong, Q.; Fang, Y.; Shao, Y.; Mulligan, P.; Qiu, J.; Cao, L.; Huang, J. Electron-Hole Diffusion Lengths > 175 Mm in Solution-Grown CH3NH3PbI3 Single Crystals. *Science* **2015**, *347*, 967−970.
(5) Yang, W. S.; Noh, J. H.; Jeon, N. J.; Kim, Y. C.; Ryu, S.; Seo, J.; Seok, S. I. High-Performance Photovoltaic Perovskite Layers Fabricated through Intramolecular Exchange. *Science* **2015**, *348*, 1234−1237.
(6) Stoumpos, C. C.; Malliakas, C. D.; Kanatzidis, M. G. Semiconducting Tin and Lead Iodide Perovskites with Organic Cations: Phase Transitions, High Mobilities, and Near-Infrared Photoluminescent Properties. *Inorg. Chem.* **2013**, *52*, 9019−9038.
(7) Tombe, S.; Adam, G.; Heilbrunner, H.; Apaydin, D. H.; Ulbricht, C.; Sariciftci, N. S.; Arendse, C. J.; Iwuoha, E.; Scharber, M. C. Optical and Electronic Properties of Mixed Halide (X = I, Cl, Br) Methylammonium Lead Perovskite Solar Cells. *J. Mater. Chem. C* **2017**, *5*, 1714−1723.
(8) Kojima, A.; Teshima, K.; Shirai, Y.; Miyasaka, T. Organometal Halide Perovskites as Visible-Light Sensitizers for Photovoltaic Cells. *J. Am. Chem. Soc.* **2009**, *131*, 6050−6051.
(9) NREL. Best Research-Cell Efficiency Chart. Photovoltaic Research. https://www.nrel.gov/pv/cell-efficiency.html (accessed October 11, 2019).
(10) Yin, W.-J.; Shi, T.; Yan, Y. Unusual Defect Physics in CH3NH3PbI3 Perovskite Solar Cell Absorber. *Appl. Phys. Lett.* **2014**, *104*, No. 063903.
(11) Burschka, J.; Pellet, N.; Moon, S.-J.; Humphry-Baker, R.; Gao, P.; Nazeeruddin, M. K.; Grätzel, M. Sequential Deposition as a Route to High-Performance Perovskite-Sensitized Solar Cells. *Nature* **2013**, *499*, 316−319.
(12) Lee, M. M.; Teuscher, J.; Miyasaka, T.; Murakami, T. N.; Snaith, H. J. Efficient Hybrid Solar Cells Based on Meso-Superstructured Organometal Halide Perovskites. *Science* **2012**, *338*, 643−647.
(13) Rodríguez-Romero, J.; Sanchez-Diaz, J.; Echeverría-Arrondo, C.; Masi, S.; Esparza, D.; Barea, E. M.; Mora-Seró, I. Widening the 2D/3D Perovskite Family for Efficient and Thermal-Resistant Solar Cells by the Use of Secondary Ammonium Cations. *ACS Energy Lett.* **2020**, *5*, 1013−1021.
(14) Torres, J.; Sanchez-Diaz, J.; Rivas, J. M.; Torre, J. de. la.; Zarazua, I.; Esparza, D. Electrical Properties and J-V Modeling of Perovskite (CH3NH3PbI3) Solar Cells after External Thermal Exposure. *Sol. Energy* **2021**, *222*, 95−102.
(15) Saliba, M. Polyelemental, Multicomponent Perovskite Semiconductor Libraries through Combinatorial Screening. *Adv. Energy Mater.* **2019**, *9*, No. 1803754.
(16) Zhang, Y.; Xu, X. Machine Learning Lattice Constants for Cubic Perovskite Compounds. *ChemistrySelect* **2020**, *5*, 9999−10009.
(17) Li, M.; Li, H.; Fu, J.; Liang, T.; Ma, W. Recent Progress on the Stability of Perovskite Solar Cells in a Humid Environment. *J. Phys. Chem. C* **2020**, *124*, 27251−27266.
(18) Tress, W.; Domanski, K.; Carlsen, B.; Agarwalla, A.; Alharbi, E. A.; Graetzel, M.; Hagfeldt, A. Performance of Perovskite Solar Cells under Simulated Temperature-Illumination Real-World Operating Conditions. *Nat. Energy* **2019**, *4*, 568−574.
(19) Turren-Cruz, S.-H.; Hagfeldt, A.; Saliba, M. Methylammonium-Free, High-Performance, and Stable Perovskite Solar Cells on a Planar Architecture. *Science* **2018**, *362*, 449−453.
(20) Koh, T. M.; Fu, K.; Fang, Y.; Chen, S.; Sum, T. C.; Mathews, N.; Mhaisalkar, S. G.; Boix, P. P.; Baikie, T. Formamidinium-Containing Metal-Halide: An Alternative Material for Near-IR Absorption Perovskite Solar Cells. *J. Phys. Chem. C* **2014**, *118*, 16458−16462.
(21) Saliba, M.; Matsui, T.; Seo, J.-Y.; Domanski, K.; Correa-Baena, J.-P.; Nazeeruddin, M. K.; Zakeeruddin, S. M.; Tress, W.; Abate, A.; Hagfeldt, A.; Grätzel, M. Cesium-Containing Triple Cation Perovskite Solar Cells: Improved Stability, Reproducibility and High Efficiency. *Energy Environ. Sci.* **2016**, *9*, 1989−1997.
(22) Saliba, M.; Matsui, T.; Domanski, K.; Seo, J.-Y.; Ummadisingu, A.; Zakeeruddin, S. M.; Correa-Baena, J.-P.; Tress, W. R.; Abate, A.; Hagfeldt, A.; Grätzel, M. Incorporation of Rubidium Cations into Perovskite Solar Cells Improves Photovoltaic Performance. *Science* **2016**, *354*, 206−209.
(23) Tang, Z.; Bessho, T.; Awai, F.; Kinoshita, T.; Maitani, M. M.; Jono, R.; Murakami, T. N.; Wang, H.; Kubo, T.; Uchida, S.; Segawa, H. Hysteresis-Free Perovskite Solar Cells Made of Potassium-Doped Organometal Halide Perovskite. *Sci. Rep.* **2017**, *7*, No. 12183.
(24) Turren-Cruz, S.-H.; Saliba, M.; T Mayer, M.; Juárez-Santiesteban, H.; Mathew, X.; Nienhaus, L.; Tress, W.; P Erodici, M.; Sher, M.-J.; G Bawendi, M.; Grätzel, M.; Abate, A.; Hagfeldt, A.; Correa-Baena, J.-P. Enhanced Charge Carrier Mobility and Lifetime Suppress Hysteresis and Improve Efficiency in Planar Perovskite Solar Cells. *Energy Environ. Sci.* **2018**, *11*, 78−86.
(25) Wang, M.; Wang, W.; Ma, B.; Shen, W.; Liu, L.; Cao, K.; Chen, S.; Huang, W. Lead-Free Perovskite Materials for Solar Cells. *Nano−Micro Lett.* **2021**, *13*, 62.
(26) Heo, J. H.; Song, D. H.; Im, S. H. Planar CH3NH3PbBr3 Hybrid Solar Cells with 10.4% Power Conversion Efficiency, Fabricated by Controlled Crystallization in the Spin-Coating Process. *Adv. Mater.* **2014**, *26*, 8179−8183.
(27) Prajongtat, P.; Dittrich, T. Precipitation of CH3NH3PbCl3 in CH3NH3PbI3 and Its Impact on Modulated Charge Separation. *J. Phys. Chem. C* **2015**, *119*, 9926−9933.
(28) Correa-Baena, J.-P.; Saliba, M.; Buonassisi, T.; Grätzel, M.; Abate, A.; Tress, W.; Hagfeldt, A. Promises and Challenges of Perovskite Solar Cells. *Science* **2017**, *358*, 739−744.
(29) Bi, D.; Tress, W.; Dar, M. I.; Gao, P.; Luo, J.; Renevier, C.; Schenk, K.; Abate, A.; Giordano, F.; Correa Baena, J.-P.; Decoppet, J.-D.; Zakeeruddin, S. M.; Nazeeruddin, M. K.; Grätzel, M.; Hagfeldt, A. Efficient Luminescent Solar Cells Based on Tailored Mixed-Cation Perovskites. *Sci. Adv.* **2016**, *2*, No. e1501170.
(30) Kim, J. Y.; Lee, J.-W.; Jung, H. S.; Shin, H.; Park, N.-G. High-Efficiency Perovskite Solar Cells. *Chem. Rev.* **2020**, *120*, 7867−7918.
(31) Al-Ashouri, A.; Köhnen, E.; Li, B.; Magomedov, A.; Hempel, H.; Caprioglio, P.; Márquez, J. A.; Vilches, A. B. M.; Kasparavicius, E.; Smith, J. A.; Phung, N.; Menzel, D.; Grischek, M.; Kegelmann, L.; Skroblin, D.; Gollwitzer, C.; Malinauskas, T.; Jošt, M.; Matič, G.; Rech, B.; Schlatmann, R.; Topič, M.; Korte, L.; Abate, A.; Stannowski, B.; Neher, D.; Stolterfoht, M.; Unold, T.; Getautis, V.; Albrecht, S. Monolithic Perovskite/Silicon Tandem Solar Cell with >29% Efficiency by Enhanced Hole Extraction. *Science* **2020**, *370*, 1300−1309.
(32) Zarazúa, I.; Sidhik, S.; Lopéz-Luke, T.; Esparza, D.; De la Rosa, E.; Reyes-Gomez, J.; Mora-Seró, I.; Garcia-Belmonte, G. Operating Mechanisms of Mesoscopic Perovskite Solar Cells through Impedance Spectroscopy and J−V Modeling. *J. Phys. Chem. Lett.* **2017**, *8*, 6073−6079.

https://doi.org/10.1021/acsaem.2c02161
ACS Appl. Energy Mater. 2022, 5, 12545−12552

(33) Zarazua, I.; Han, G.; Boix, P. P.; Mhaisalkar, S.; Fabregat-Santiago, F.; Mora-Seró, I.; Bisquert, J.; Garcia-Belmonte, G. Surface Recombination and Collection Efficiency in Perovskite Solar Cells from Impedance Analysis. *J. Phys. Chem. Lett.* **2016**, *7*, 5105−5113.
(34) Fabregat-Santiago, F.; Garcia-Belmonte, G.; Mora-Seró, I.; Bisquert, J. Characterization of Nanostructured Hybrid and Organic Solar Cells by Impedance Spectroscopy. *Phys. Chem. Chem. Phys.* **2011**, *13*, 9083−9118.
(35) Guerrero, A.; Bisquert, J.; Garcia-Belmonte, G. Impedance Spectroscopy of Metal Halide Perovskite Solar Cells from the Perspective of Equivalent Circuits. *Chem. Rev.* **2021**, *121*, 14430−14484.
(36) Hubbard, S.Absorption and Generation. In *Photovoltaic Solar Energy*, John Wiley & Sons, Ltd., 2016; pp 32−38.
(37) Ono, L. K.; Juarez-Perez, E. J.; Qi, Y. Progress on Perovskite Materials and Solar Cells with Mixed Cations and Halide Anions. *ACS Appl. Mater. Interfaces* **2017**, *9*, 30197−30246.
(38) Pitarch-Tena, D.; Ngo, T. T.; Vallés-Pelarda, M.; Pauporté, T.; Mora-Seró, I. Impedance Spectroscopy Measurements in Perovskite Solar Cells: Device Stability and Noise Reduction. *ACS Energy Lett.* **2018**, *3*, 1044−1048.
(39) Yoo, S.-M.; Yoon, S. J.; Anta, J. A.; Lee, H. J.; Boix, P. P.; Mora-Seró, I. An Equivalent Circuit for Perovskite Solar Cell Bridging Sensitized to Thin Film Architectures. *Joule* **2019**, *3*, 2535−2549.
(40) Riquelme, A. J.; Valadez-Villalobos, K.; Boix, P. P.; Oskam, G.; Mora-Seró, I.; Anta, J. A. Understanding Equivalent Circuits in Perovskite Solar Cells. Insights from Drift-Diffusion Simulation. *Phys. Chem. Chem. Phys.* **2022**, *24*, 15657−15671.
(41) Contreras-Bernal, L.; Ramos-Terrón, S.; Riquelme, A.; Boix, P. P.; Idígoras, J.; Mora-Seró, I.; Anta, J. A. Impedance Analysis of Perovskite Solar Cells: A Case Study. *J. Mater. Chem. A* **2019**, *7*, 12191−12200.
(42) Moia, D.; Gelmetti, I.; Calado, P.; Fisher, W.; Stringer, M.; Game, O.; Hu, Y.; Docampo, P.; Lidzey, D.; Palomares, E.; Nelson, J.; Barnes, P. R. F. Ionic-to-Electronic Current Amplification in Hybrid Perovskite Solar Cells: Ionically Gated Transistor-Interface Circuit Model Explains Hysteresis and Impedance of Mixed Conducting Devices. *Energy Environ. Sci.* **2019**, *12*, 1296−1308.
(43) Zarazua, I.; Bisquert, J.; Garcia-Belmonte, G. Light-Induced Space-Charge Accumulation Zone as Photovoltaic Mechanism in Perovskite Solar Cells. *J. Phys. Chem. Lett.* **2016**, *7*, 525−528.
(44) Riquelme, A.; Bennett, L. J.; Courtier, N. E.; Wolf, M. J.; Contreras-Bernal, L.; Walker, A. B.; Richardson, G.; Anta, J. A. Identification of Recombination Losses and Charge Collection Efficiency in a Perovskite Solar Cell by Comparing Impedance Response to a Drift-Diffusion Model. *Nanoscale* **2020**, *12*, 17385−17398.
(45) Calado, P.; Burkitt, D.; Yao, J.; Troughton, J.; Watson, T. M.; Carnie, M. J.; Telford, A. M.; O'Regan, B. C.; Nelson, J.; Barnes, P. R. F. Identifying Dominant Recombination Mechanisms in Perovskite Solar Cells by Measuring the Transient Ideality Factor. *Phys. Rev. Appl.* **2019**, *11*, No. 044005.
(46) Wolff, C. M.; Caprioglio, P.; Stolterfoht, M.; Neher, D. Nonradiative Recombination in Perovskite Solar Cells: The Role of Interfaces. *Adv. Mater.* **2019**, *31*, No. 1902762.
(47) Velilla, E.; Jaramillo, F.; Mora-Seró, I. High-Throughput Analysis of the Ideality Factor to Evaluate the Outdoor Performance of Perovskite Solar Minimodules. *Nat. Energy* **2021**, *6*, 54−62.
(48) Courtier, N. E. Interpreting Ideality Factors for Planar Perovskite Solar Cells: Ectypal Diode Theory for Steady-State Operation. *Phys. Rev. Appl.* **2020**, *14*, No. 024031.
(49) Castro-Chong, A.; Riquelme, A. J.; Aernouts, T.; Bennett, L. J.; Richardson, G.; Oskam, G.; Anta, J. A. Illumination Intensity Dependence of the Recombination Mechanism in Mixed Perovskite Solar Cells. *ChemPlusChem* **2021**, *86*, 1347−1356.
(50) Tress, W.; Yavari, M.; Domanski, K.; Yadav, P.; Niesen, B.; Baena, J. P. C.; Hagfeldt, A.; Graetzel, M. Interpretation and Evolution of Open-Circuit Voltage, Recombination, Ideality Factor and Subgap Defect States during Reversible Light-Soaking and Irreversible Degradation of Perovskite Solar Cells. *Energy Environ. Sci.* **2018**, *11*, 151−165.
(51) Park, N.-G.; Grätzel, M.; Miyasaka, T.*Organic−Inorganic Halide Perovskite Photovoltaics: From Fundamentals to Device Architectures*, Springer International Publishing, 2016.
(52) Marinova, N.; Tress, W.; Humphry-Baker, R.; Dar, M. I.; Bojinov, V.; Zakeeruddin, S. M.; Nazeeruddin, M. K.; Grätzel, M. Light Harvesting and Charge Recombination in CH3NH3PbI3 Perovskite Solar Cells Studied by Hole Transport Layer Thickness Variation. *ACS Nano* **2015**, *9*, 4200−4209.

https://doi.org/10.1021/acsaem.2c02161
ACS Appl. Energy Mater. 2022, 5, 12545−12552